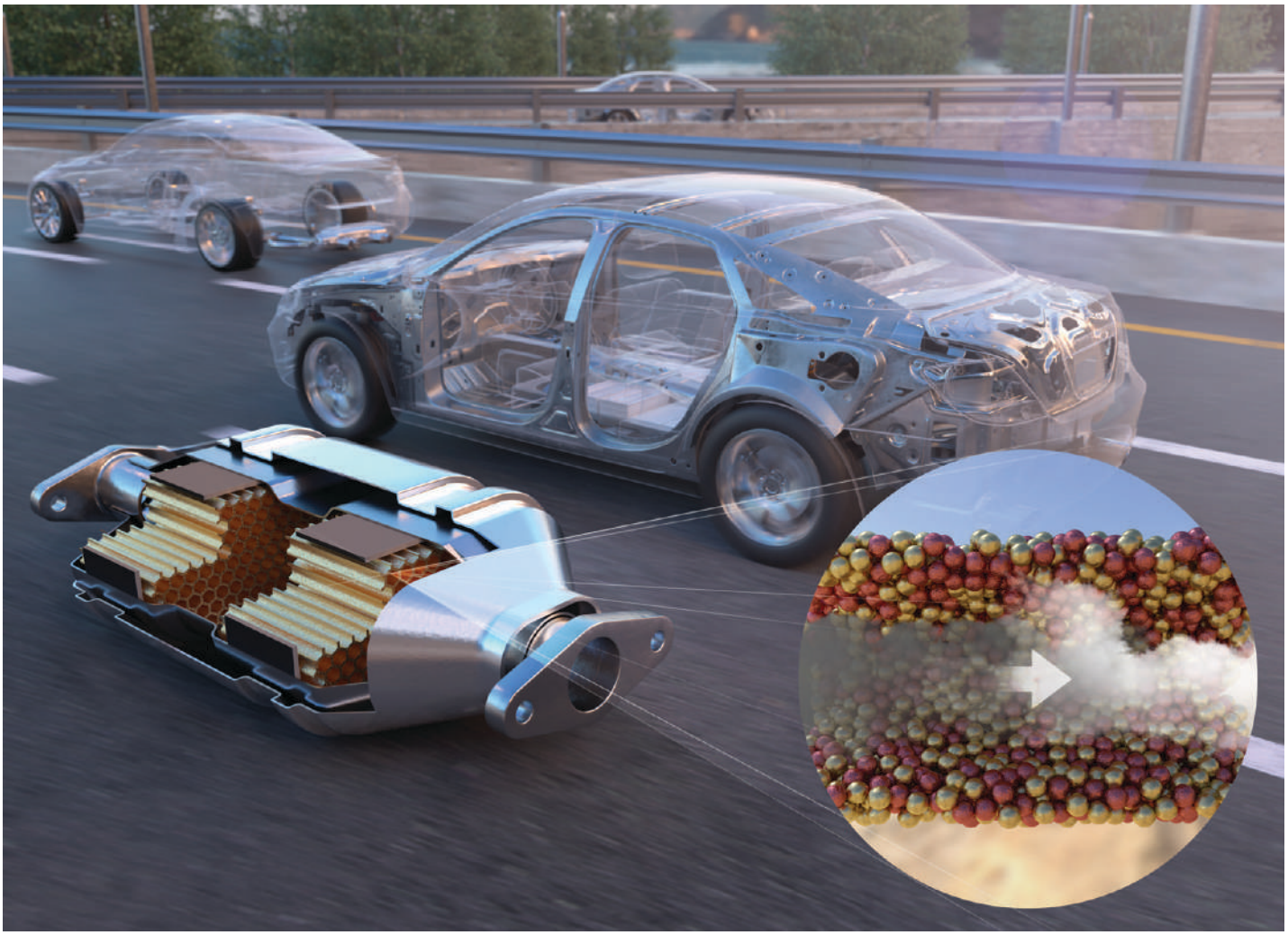

Showcasing research from Dr Seok Ki Kim's laboratory at Korea Research Institute of Chemical Technology.

A first-principles understanding of the CO-assisted NO reduction on the $IrRu/Al_2O_3$ catalyst under O_2-rich conditions

$IrRu/Al_2O_3$ shows excellent NO_x reduction performance under lean-burn conditions (O_2-rich) without using urea. The atomic-scale understanding of the superior performance of the IrRu alloy is provided. A design strategy for the cost-efficient catalyst synthesis is also suggested.

As featured in:

See Iljeong Heo, Seok Ki Kim *et al.*, *Catal. Sci. Technol.*, 2021, **11**, 4353.

ROYAL SOCIETY OF CHEMISTRY

rsc.li/catalysis

Registered charity number: 207890

Catalysis Science & Technology

ROYAL SOCIETY OF CHEMISTRY

PAPER

View Article Online
View Journal | View Issue

Check for updates

Cite this: *Catal. Sci. Technol.*, 2021, 11, 4353

A first-principles understanding of the CO-assisted NO reduction on the IrRu/Al_2O_3 catalyst under O_2-rich conditions†

Malik Waqar Arshad, [ab] Dong Hun Kim,[c] Young-Woo You,[cd] Soo Min Kim,[bcd] Iljeong Heo *[cd] and Seok Ki Kim *[ab]

Received 27th April 2021,
Accepted 4th June 2021

DOI: 10.1039/d1cy00744k

rsc.li/catalysis

Controlling the surface composition of alloy catalysts can provide an opportunity to improve their activity and selectivity for a target reaction. However, since the various effects of alloys are often mixed, it is difficult to maximize the expected benefits of the alloy formation. In the present study, we prepared an IrRu bimetallic catalyst by using a wetness impregnation method and studied the reaction performance of NO reduction by CO in the presence and absence of O_2. A series of spectroscopic analyses confirmed the formation of the IrRu bimetallic alloy. Further, we investigate the active-site ensemble effect in the IrRu bimetallic catalyst that selectively reduces NO to N_2 using CO as a reducing agent in the presence of excess oxygen. Mechanistic insight gained through the density functional theory calculations revealed that the IrRu alloy catalyst has moderate binding energies for all the adsorbates and intermediates, resulting in the acceleration of critical surface reactions, such as CO oxidation and N–NO disproportionation. In addition, a series of theoretical surface models suggest that the selectivity promotion on the IrRu alloy surface originates from the ensemble effect, while ligand and strain effects are detrimental to the catalyst performance. This study lays the foundation for the design of bimetallic catalysts that can provide maximal promotion of NO reduction with minimal use of precious metals.

1. Introduction

Nitrogen oxides (NO_x) are emitted in large quantities from various industrial processes and vehicle exhaust. NO_x are not only hazardous to human health because of their toxicity, but also harmful to ecosystems and the atmosphere because they cause ozone layer depletion and acid rain.[1–4] Selective catalytic reduction has been widely accepted as a commercial technology for automotive sectors, particularly urea selective catalytic reduction (SCR), in which ammonia is used as a reducing agent to reduce NO_x under O_2-rich conditions. Furthermore, this method meets all EURO-VI emission standards.[5] Despite the excellent performance of this ammonia-based SCR, it has some disadvantages that need to be addressed. For instance, ammonia slippage could occur, which produces $PM_{2.5}$ air pollutants. Moreover, the use of urea leads to high operational costs, its dosage in the SCR system is difficult to control, and it decomposes at a low temperature of 200 °C.[6,7] To overcome these problems, many researchers are trying to find alternative, non-urea-based reductants for SCR.[8,9]

The CO-assisted SCR (CO-SCR) of NO is more attractive than the urea-based SCR because CO is generally present in vehicle exhaust and can be more easily produced by engine operation compared with other exhaust components, such as H_2. Moreover, recently developed internal combustion engines, such as homogeneous charge compression ignition (HCCI) engines, emit relatively high concentrations of CO,[10] which can be used as a reductant for NO. The catalytic reduction of NO by CO is an important process for automobile exhaust abatement, which requires the catalyst to have good catalytic activity, high selectivity for N_2, and good catalytic stability under a reductive atmosphere at temperatures from 150 °C up to 700 °C. The removal of NO_x from oxygen-rich exhaust is extremely difficult for conventional three-way catalysts (TWCs), as they are designed for gasoline engine exhaust treatment. Diesel engines must

[a] *C1 Gas & Carbon Convergent Research Center, Korea Research Institute of Chemical Technology (KRICT), 141 Gajeong-ro, Yuseong-gu, Daejeon 34114, Republic of Korea. E-mail: skkim726@krict.re.kr*
[b] *University of Science & Technology, Advanced Materials and Chemical Engineering Technology (UST), 217 Gajeong-ro, Yuseong-gu, Daejeon 34113, Republic of Korea*
[c] *Environment & Sustainable Resources Research Center, Korea Research Institute of Chemical Technology (KRICT), 141 Gajeong-ro, Yuseong-gu, Daejeon 34114, Republic of Korea. E-mail: zaiseok@krict.re.kr*
[d] *Convergent Chemistry of Air Pollution Center, Korea Research Institute of Chemical Technology (KRICT), 141 Gajeong-ro, Yuseong-gu, Daejeon 34114, Republic of Korea*

† Electronic supplementary information (ESI) available: Detailed methods (DFT calculations) and corresponding additional data. See DOI: 10.1039/d1cy00744k

be operated in a very narrow, lean-burn range to use TWCs, and this is a major obstacle preventing the improvement of their fuel efficiency. This situation has prompted research into the development of a new catalyst technology that is capable of reducing diesel engine NO_x emissions under lean-burn conditions.[11–14] Owing to the very strict requirements of EURO-VI, only precious-metal nanoparticles (*e.g.*, Pt, Pd, and Rh) supported on honeycomb ceramics are commercially used for gasoline engine exhaust treatment. However, there is plenty of potential to replace urea-SCR for diesel exhaust aftertreatments.[1,15,16]

Platinum group metals (PGMs) such as Ir, Ru, Rh, Pt, and Pd are known as efficient catalysts for NO reduction with CO,[17,18] H_2,[19] NH_3,[20] and hydrocarbons[21] serving as reductants. CO-SCR was first reported by Tauster and Murrell,[22] who measured the catalytic activity of 0.1% Ir/Al_2O_3 (0.1 g) for CO-SCR using a reaction gas mixture composed of 0.2% NO, 1.0% CO, and 0.75% O_2 diluted in He (flow rate of 100 L h^{-1}). They reported that the NO conversion was as high as 90% at 400 °C. This indicates that NO preferentially reacts with CO over O_2. The interesting catalytic performance of Ir/Al_2O_3 was explained by NO molecules being more likely to adsorb onto a surface site than O_2 molecules. Other reports[8,22–26] suggest that Ir is a promising catalytic component for CO-SCR. Despite the good activity of Ir, it has a rather high light-off temperature (T_{50}) under lean-burn conditions. Bimetallic alloys can overcome this problem, as the second metal can electronically promote monometallic Ir and express significant synergistic effects. In fact, a previous report details an alloy synergistic effect that increased the catalyst activity for NO reduction by CO.[18] Ru is a potential promoter candidate for alloy formation with Ir as it offers good O_2 tolerance and a low light-off temperature under lean-burn conditions.[27–29]

The mechanism of NO reduction on the surface of PGMs has been extensively studied, and the following process (eqn (1)–(7)) is generally accepted:[18,21,29–32]

$$NO \rightarrow N + O \text{ (NO dissociation)} \quad (1)$$

$$N + N \rightarrow N_2 \text{ (N_2 formation)} \quad (2)$$

$$N + NO \rightarrow N_2O \text{ (side reaction)} \quad (3)$$

$$N_2O \rightarrow N_2 + O \text{ (N_2O decomposition)} \quad (4)$$

$$NO + N \rightarrow N_2 + O \text{ (NO disproportionation)} \quad (5)$$

$$NO + O \rightarrow NO_2 \text{ (side reaction)} \quad (6)$$

$$O + R \rightarrow RO \text{ (oxygen consumption, R = CO or } H_2) \quad (7)$$

Hence, the suppression of the reactions in eqn (3) and (6) and/or the promotion of the reactions in eqn (4) and (7) are required to develop a highly selective NO reduction system. Theoretical approaches have also been made to predict the catalytic activity of PGMs and suggested that a stepped (211) and/or (111) surface could suppress the reactions in eqn (3) and (6).[33,34]

Alloy formation can affect the catalytic activity and selectivity in different ways, altering the geometric or electronic properties of the system.[35,36] In our previous study,[29] an IrRu/Al_2O_3 catalyst exhibited an outstanding performance in the selective, lean NO_x reduction by CO. Although various experimental approaches have revealed the alloy formation and catalytic properties of the IrRu/Al_2O_3 catalyst, the origin of its improved catalytic performance has not yet been identified. In the present study, we synthesized the IrRu/Al_2O_3 catalyst again and confirmed its lean NO_x reduction performance according to temperature change. Furthermore, we modeled a series of Ir, Ru, and IrRu-alloy surfaces using density functional theory (DFT) to elucidate the origin of the performance changes due to alloy formation. Through this, we quantified the extent to which the ligand, strain, and ensemble effects significantly contributed to the improvement of the catalytic performance. These findings may provide a basis for designing more active and selective catalysts through the tuning of their elementary reaction energetics.[37–39]

2. Materials and methods

2.1 Materials

All chemicals were purchased from commercial sources and used without further purification. Iridium(III) chloride hydrate ($IrCl_3$), ruthenium(III) chloride hydrate ($RuCl_3$), and γ-alumina (γ-Al_2O_3, pore volume of 0.43 mL g^{-1}) were purchased from Strem Chemicals, Inc. The water used in this experiment was deionized using a Synergy® UV water purification system.

2.2 Catalyst preparation

Catalysts were prepared by the incipient wetness impregnation method with a total metal loading of 5 wt%. An appropriate amount of an $IrCl_3$ (or $RuCl_3$) aqueous solution was added dropwise to γ-Al_2O_3. The resultant product was dried at 80 °C overnight and calcined at 500 °C for 5 h under N_2 and an absolute humidity of 93.3 g m^{-3}, which was designed to completely remove any Cl species on the catalyst surface.

2.3 Characterization

High-resolution powder X-ray diffraction (HR-PXRD) patterns were obtained with an X-ray diffractometer (Rigaku Smart Lab) operated at 45 kV and 200 mA using a Cu Kα radiation source with a wavelength of 1.5418 Å. The diffraction patterns were recorded in the 2θ range of 10–90° with a step size of 0.02°. The patterns were matched to the Joint Committee on Powder Diffraction Standards (JCPDS) data.

High-resolution transmission electron microscopy (HR-TEM) and high-angle annular dark-field scanning TEM

(HAADF-STEM) with elemental mapping were conducted using a Titan cubed G2 60–300 instrument with an acceleration voltage of 200 kV. The sample was dispersed in EMSURE® ethanol with ultrasonic treatment, and the resulting suspension was dried on carbon-coated TEM grids.

2.4 Catalyst activity test

The NO_x reduction performance of the prepared catalysts was evaluated in a conventional packed-bed flow reactor with an inner diameter of 10 mm. A 0.45 mL sample of the catalyst (particle size of 300–600 μm) was placed in the middle of the reactor, and an advanced engine reaction stream consisting of 50 ppm NO, 0.7% CO, and 5% O_2 balanced with N_2 was fed with a gas hourly space velocity (GHSV) of 100 000 h^{-1}. An O_2-free reactant gas mixture was also used to evaluate the oxygen resistance of the catalyst. The reaction temperature was continuously increased from 100 °C to 500 °C at a rate of 2 °C min^{-1}. Prior to the activity test, the catalyst was reduced under 10% H_2/N_2 at 450 °C for 2 h. Gas concentrations were quantified using a Fourier-transform infrared (FT-IR, Nicolet iS 10, Thermo Fisher Scientific) spectrometer equipped with a gas cell with a 2 m path length (Thermo Fisher Scientific) and a deuterated triglyceride sulfate (DTGS) detector. The NO_x concentration, CO conversion, and the selectivities to NO_2 and N_2 were calculated using the following equations (eqn (8)–(11)):

$$\text{NO}_x \text{ concentration } ([\text{NO}_x]) = [\text{NO}] + [\text{NO}_2] \quad (8)$$

$$\text{NO}_x/\text{CO Conversion } (\%) = \frac{[\text{X}]_{\text{in}} - [\text{X}]_{\text{out}}}{[\text{X}]_{\text{in}}} \times 100 \quad (9)$$

$$\text{NO}_2 \text{ selectivity } (\%) = \frac{[\text{NO}_2]_{\text{out}}}{[\text{NO}]_{\text{in}} - [\text{NO}]_{\text{out}}} \times 100 \quad (10)$$

$$\text{N}_2 \text{ selectivity } (\%) = \left(1 - \frac{[\text{NO}_2]_{\text{out}} + 2 \times [\text{N}_2\text{O}]_{\text{out}} + [\text{NH}_3]_{\text{out}}}{[\text{NO}]_{\text{in}} - [\text{NO}]_{\text{out}}}\right) \times 100 \quad (11)$$

Here, [X] represents the concentration of NO_x or CO.

2.5 Computational details

The mechanistic investigation into NO_x reduction on active metal surfaces was conducted using DFT with a plane-wave basis set, as implemented in the Vienna *ab-initio* simulation package (VASP).[40,41] The vdW-DF2 exchange–correlation functional in the generalized gradient approximation was employed,[42–44] and the kinetic energy cutoff was set to 450 eV. For the bulk and surface slab calculations, the Brillouin zone samplings were carried out using Monkhorst–Pack *k*-point mesh grids of 16 × 16 × 16 and 4 × 4 × 1, respectively. The Gibbs free energies (G) of the gas molecules were calculated under the assumption that they were ideal gases; thus, their vibrational, translational, and rotational degrees of freedom were considered using the following equation (eqn (12)):

$$G_{\text{gas}}(T,P) = E_{\text{elec}} + E_{\text{ZPE}} + \int_0^T C_{\text{p}} dT - TS(T,P), \quad (12)$$

where E_{elec} is the electronic energy, E_{ZPE} is the zero-point energy, C_{p} is the constant-pressure heat capacity, and S is the entropy. On the other hand, the ΔG of the adsorbent was calculated under a harmonic limit, in which only the vibrational degree of freedom was considered, using the following equation (eqn (13)):

$$G_{\text{adsorbate}}(T,P) = E_{\text{elec}} + E_{\text{ZPE}} + \sum_i^{3N} \frac{\varepsilon_{\text{i}}}{e^{\varepsilon_{\text{i}}/k_{\text{B}}T} - 1} - TS(T), \quad (13)$$

where N is the number of atoms, ε_{i} is the energy associated with the vibrational frequencies, and k_{B} is the Boltzmann constant. E_{elec}, E_{ZPE}, C_{p}, and S were obtained using the thermodynamic partition function, which is well documented in the literature.[45] Face-centered cubic Ir (111)[46] and hexagonal close-packed Ru (001)[47] phases were chosen for the model surface structures because they exhibited the lowest surface energies among the corresponding surface structures. A 4 × 4 × 1 atomic surface slab with four atomic layers was constructed to simulate the Ir (111) and Ru (001) surfaces (see Fig. S1 in the ESI†). The bottom two layers were fixed at a bulk equilibrium position while the surface two layers were optimized by the electronic structure. A vacuum thickness of 15 Å was applied for all the surface slab models. To simulate the IrRu alloy system, Ru-doped Ir (Ir_3Ru_1) and Ir-doped Ru (Ir_1Ru_3) structures were constructed with 25% dopant concentration (see Fig. S2 in the ESI†). To determine the catalyst intrinsic activity, electronic and geometric effect studies were carried out by studying the ligand-, strain-, and ensemble-effect phenomena.[48,49] The O_2-rich conditions were simulated by adding an oxygen atom to the adjacent site of the adsorbates (see Fig. S3 in the ESI†). The binding energy of an adsorbate (A) to a catalyst surface was calculated in terms of the free energy of adsorption using the following equation (eqn (14)):

$$G_{\text{B.E. of A}} = G_{\text{surface+A}} - (G_{\text{surface}} + G_{\text{A}}), \quad (14)$$

where $G_{\text{surface+A}}$, G_{surface}, and G_{A} denote the free energies of the total adsorbed system, the relaxed clean surface, and the gas phase molecule A, respectively. We report the adsorption energies at the most stable site after testing various adsorption sites.

The transition-state energies for the CO–O, N–O, N–CO, N–N, NO–N, O–O, NO–O, C–O, and N_2–O bond formation (or decomposition) steps on the Ir (111), Ru (001), Ir_3Ru_1 (111), and Ir_1Ru_3 (001) catalyst surfaces were determined using the climbing-image nudged elastic band (CI-NEB) and dimer methods[50–52] (see Fig. S24–S32 in the ESI†). All the transition states were verified by the vibrational frequency analysis at the saddle point showing single imaginary frequency.

3. Results and discussion

3.1 Catalyst structure

Fig. 1 shows the HR-PXRD patterns of the catalysts prepared in the present study. The Ir/Al_2O_3 and Ru/Al_2O_3 catalysts showed typical face-centered cubic and hexagonal close-packed structures, respectively, for their corresponding metal crystals. Ir/Al_2O_3 showed sharp peaks at 2θ values of 40.6°, 47.2°, and 69.1°, indicating that metallic Ir possesses a large crystallite size (31.6 nm calculated from Ir(111)). Contrastingly, Ru/Al_2O_3 showed broad peaks at 2θ values of 42.3°, 44.1°, and 84.7°, indicating that the crystallite size of Ru is relatively small (8.3 nm calculated from Ru(101)). In the case of the $IrRu/Al_2O_3$ catalyst, the distinct peaks belonging to the Ir and Ru crystals disappeared, and broad peaks were observed between the Ir and Ru peaks. For instance, the peaks shown at 40.9° and 83.2° of the $IrRu/Al_2O_3$ are located between Ir(111) and Ru(101), and between Ir(211) and Ru(212), respectively. This suggests that lattice expansion or shrinkage occurs because of the IrRu alloy formation. The estimated lattice constants of $IrRu/Al_2O_3$ based on the hexagonal close-packed structure are summarized in Table 1.

HR-TEM analysis was also carried out for the reduced catalysts to observe the alloy formation phenomena (Fig. 2). As expected, the HR-TEM image of the Ir/Al_2O_3 catalyst showed large Ir crystals that grew in one direction, resulting in a rod-like structure. The length of the longer direction was greater than 300 nm. The Ru particles of Ru/Al_2O_3 were much smaller than the Ir particles of Ir/Al_2O_3, appearing in lumped clusters with a size of approximately 300 nm. However, the metal particles of the $IrRu/Al_2O_3$ catalyst were even smaller than those of the Ru/Al_2O_3 catalyst. The lattice spacing and energy-dispersive X-ray spectroscopy (EDS) mapping indicated the formation of the IrRu bimetallic catalyst system. That is, the lattice spacing of the metallic particles of $IrRu/Al_2O_3$ was 2.2 Å, which was not defined in both pure Ir and Ru structures, and EDS shows that Ir and Ru are well mixed in the same observation region.

3.2 Catalyst activity

The CO-assisted NO reduction activities of the prepared catalysts were observed with and without the presence of O_2. The NO conversion as a function of temperature without O_2 is shown in Fig. 3. For Ru/Al_2O_3, NO was converted to N_2 at a temperature of 100 °C and reached 100% conversion at 210 °C. $IrRu/Al_2O_3$ showed similar behavior to Ru/Al_2O_3 but provided the same conversion of NO at a temperature 10–20 °C higher than that required by Ru/Al_2O_3. The activity of Ir/Al_2O_3 was the lowest among the three catalysts, converting only half of NO at a temperature (T_{50}) of 290 °C, at which both the Ru and IrRu catalysts showed 100% NO conversion. We noted that CO converted NO to N_2 without any side products, such as N_2O or NO_2, which was not seen with the other catalysts prepared in the present study. Since the CO concentration was much higher than that of NO, CO conversion was almost negligible during our investigation.

The reaction results in the presence of O_2 are shown in Fig. 4(a–d). Unlike the reaction without O_2 (Fig. 3), the NO_x conversions that include both NO and NO_2 consumption exhibited two peaks at *ca.* 200 °C and *ca.* 400 °C for all three catalysts (Fig. 4(a)). Ir/Al_2O_3 showed the first NO_x conversion peak at 230 °C, with a maximum conversion of 59.3%. Ru/Al_2O_3 exhibited a similar trend, but the first NO_x conversion

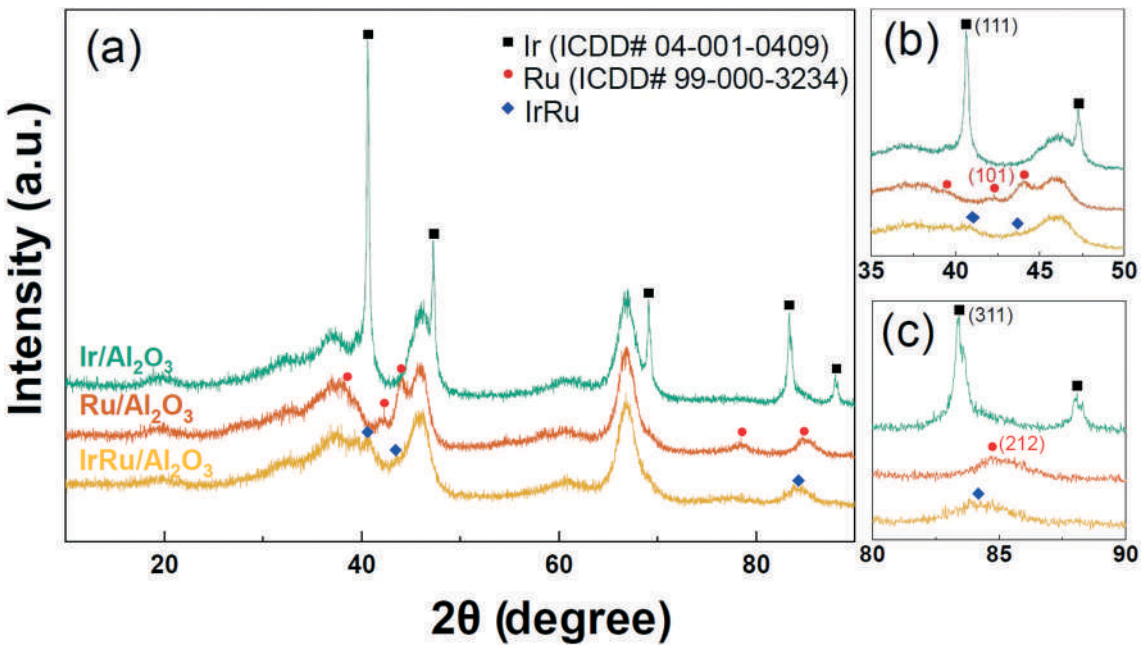

Fig. 1 High-resolution powder X-ray diffraction (PXRD) patterns of the reduced catalysts. Reduction was carried out at 450 °C for 1 h in 5% H_2. (a) Overall, (b) 35–50° enlarged, and (c) 80–90° enlarged HR-PXRD spectra.

Table 1 Comparison of the experimental and theoretical lattice constants of the catalysts

Catalyst	HR-PXRD lattice constants (Å)	Model	DFT lattice constants (Å)	Metal	Reference[a]
Ir/Al_2O_3	$a = b = c = 3.845$	Ir	$a = b = c = 3.987$	Ir (ref. 53)	$a = b = c = 3.839$
Ru/Al_2O_3	$a = b = 2.704$, $c = 4.24$	Ir_3Ru_1	$a = b = c = 3.905$	Ru (ref. 54)	$a = b = 2.705$, $c = 4.280$
$IrRu/Al_2O_3$	$a = b = 2.813$, $c = 4.394$	Ru	$a = b = 2.786$, $c = 4.397$		
		Ru_3Ir_1	$a = b = 2.801$, $c = 4.424$		

[a] Experimental values reported in previous studies.

peak shifted towards a higher temperature at approximately 260 °C. The maximum NO_x conversion of Ru/Al_2O_3 (84.6%) was higher than that of Ir/Al_2O_3, but its high performance was only observed over a narrow temperature range since the conversion rapidly decreased as the temperature rose. The NO_x conversion of $IrRu/Al_2O_3$ was also higher than that of Ir/Al_2O_3, but unlike Ru/Al_2O_3, it maintained its good performance over a wide temperature range. $IrRu/Al_2O_3$ showed a T_{50} of 160 °C and a maximum NO_x conversion of 89.6% at 212 °C. When the NO conversions were observed separately (Fig. 4(b)), they exhibited similar trends to those of NO_x, particularly for $IrRu/Al_2O_3$. The notable difference between the NO_x and NO conversions by the pure Ir and Ru catalysts was that the decreases in the NO conversion after the first peak were less significant than those seen in the NO_x conversion. The formation of NO_2 from 250 °C (Fig. 4(d)) was responsible for the decrease in the NO_x conversion.

As shown in Fig. 3, and suggested previously, CO plays an important role in NO reduction, serving as a reducing agent to remove surface O species. Thus, the CO oxidation activity of a catalyst is closely related to its low-temperature NO reduction performance. As shown in Fig. 4(c), the $IrRu/Al_2O_3$ catalyst shows 100% CO conversion at a temperature of 172 °C, which is in accordance with the temperature at which the NO reduction started and is the lowest temperature for 100% conversion among those of the catalysts prepared in this study. The temperatures for complete CO oxidation over the Ir/Al_2O_3 and Ru/Al_2O_3 catalysts were 228 °C and 254 °C, respectively, which are also consistent with the temperature at which NO reduction was activated for each catalyst.

As the reaction temperature increased above 250 °C, the NO conversion decreased for all three catalysts. This is because of the absence of CO, which was completely consumed by the formation of CO_2. As a result, surface O species were no longer removed during the reaction and they started to oxidize the surface. When the reaction temperature increased further, to above 300 °C, the oxygen concentration on the surface increased and NO began to oxidize as well, forming NO_2. It is noteworthy that the $IrRu/Al_2O_3$ catalyst started to produce NO_2 at a temperature 40–50 °C higher than those of the other catalysts, and the amount of NO_2 it produced was much smaller than that provided by the other catalysts. This suppression of this side reaction allowed the $IrRu/Al_2O_3$ catalyst to show a high NO_x conversion, even at a reaction temperature above 300 °C.

The results of the aforementioned O_2-rich NO reduction reaction are summarized as follows:

1. At temperatures below 200 °C, the NO reduction ability of a catalyst is determined by its CO oxidation activity, which removes surface O species produced by NO dissociation.

2. At temperatures above 250 °C, the absence of CO allows the surface to be oxidized and NO starts to oxidize. The suppression of this side reaction leads to a high NO_x conversion.

3. The $IrRu/Al_2O_3$ catalyst exhibited a broad temperature window for NO_x conversion due to its rapid CO oxidation and slow NO oxidation rates in the low- and high-temperature regions, respectively.

In a later section, the performance of the IrRu alloy catalyst will be discussed by comparing the DFT energetics of individual reactions associated with CO-assisted NO reduction.

3.3 DFT energetics

To study the activity and selectivity of CO-assisted NO reduction over the Ir, Ru, and IrRu-alloy catalysts, the energetics of a series of elementary reactions were analyzed using DFT calculations. Prior to the reaction energy analyses, we generated Ir- and Ru-rich alloy surface models that closely resembled the experimental surface. These were prepared by substituting 25% of the Ir or Ru bulk atoms with another element, which gave surface models Ir_3Ru_1 and Ru_3Ir_1, respectively (Fig. S1 and S2†). After DFT optimization of their bulk alloy structures, the lattice constants of Ir_3Ru_1 and Ru_3Ir_1 were changed by −2.06% and +0.58% relative to the pure Ir and Ru structures, respectively, as summarized in Table 1. Regardless of the bulk structure identified by XRD, the most stable surface orientation was expected to be exposed. Therefore, the surface orientations of Ir (and Ir-rich alloys) and Ru (and Ru-rich alloys) were chosen as (111) and (001), respectively, due to the lowest surface energy.

The reaction sequence was considered to follow the order of adsorption, intermediate formation, product formation, and desorption. Hereafter, the gas and surface species of each atom or molecule are denoted with (g) or *, respectively (*e.g.*, those of NO are denoted as NO(g) and NO*). According to a previous report,[55] the formation of O*, N*, N_2O*, and NCO* could occur; thus these species were considered as possible intermediates in our processes. NO_2(g), N_2(g), and CO_2(g) were calculated as the main gas products. In addition

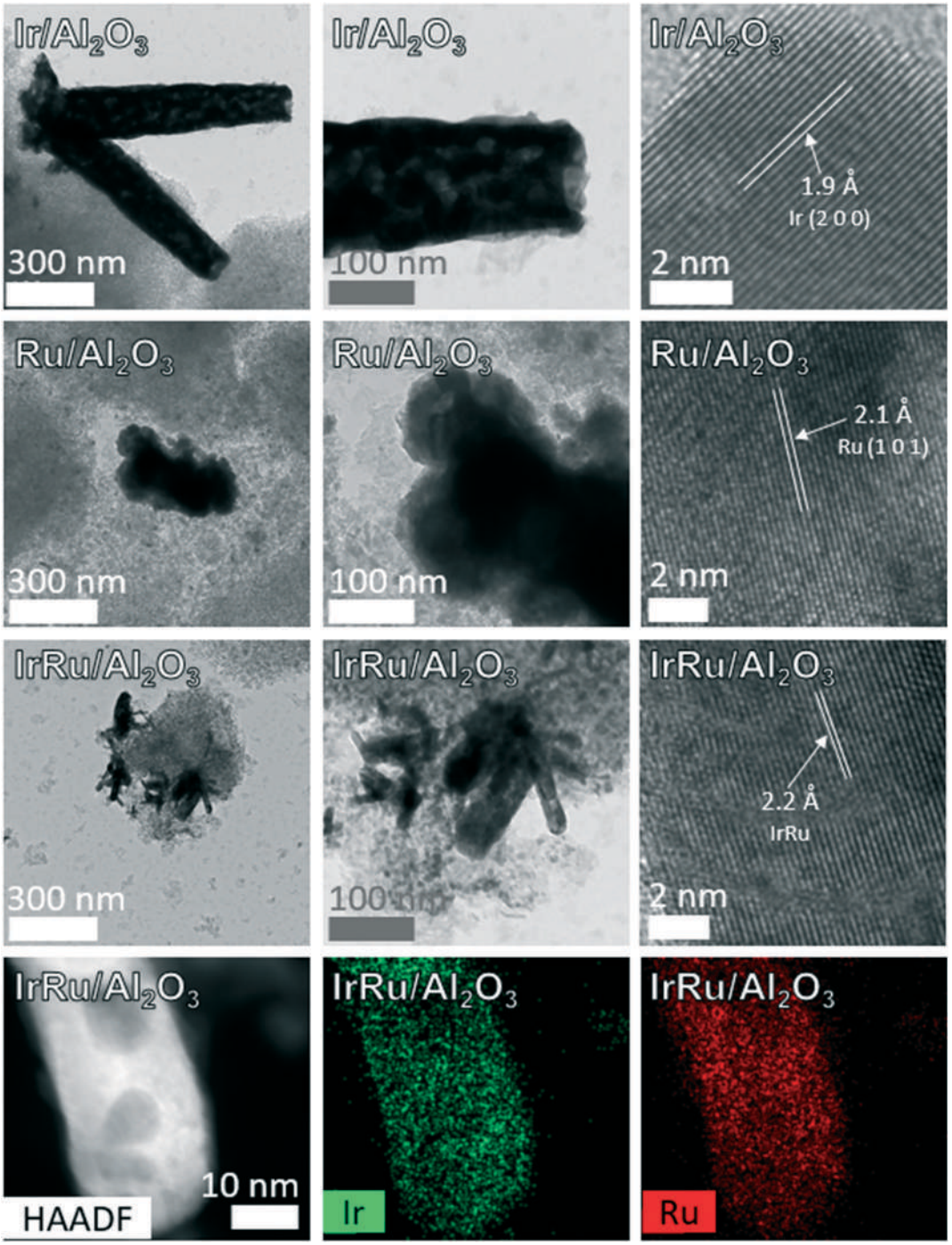

Fig. 2 High-resolution transmission electron microscopy (HR-TEM) images of the Ir/Al_2O_3, Ru/Al_2O_3, and $IrRu/Al_2O_3$ catalysts obtained after reduction at 450 °C in 10% H_2/N_2. Energy-dispersive X-ray spectroscopy (EDS) mapping results of the $IrRu/Al_2O_3$ catalyst are also shown at the bottom.

to the catalysis calculations for clean surfaces, those at sites with adjacent O* species were calculated to simulate the lean-burn (O_2-rich) conditions. The configuration of the O* adatom and the adsorption sites for the reactions are shown in Fig. S3–S7.† We note that the location of the O* adatom was not derived from the surface coverage calculations, which require additional microkinetic analysis. Instead it was placed as close as possible to an adsorbate unless they do not react with each other. However, the approach is sufficient to qualitatively describe the effect of the adjacent oxygen on the reaction energy profile. The reaction energies and corresponding activation barriers for all the elementary steps on clean and O*-covered (O_2-rich) surfaces are summarized in Table 2.

Among the four clean surfaces modeled in the present study, Ru and Ir showed the most favorable adsorption of

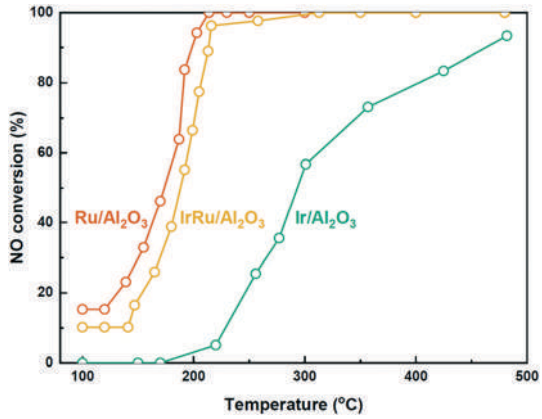

Fig. 3 NO reduction results obtained without O_2. Reaction conditions: T = 100–500 °C; P = 1 bar; 50 ppm NO, 0.7% CO balanced with N_2; GHSV = 100 000 h^{-1}.

NO(g) and CO(g), respectively. The dissociative adsorption of O_2 was calculated to be most exergonic on the Ru surface (−5.96 eV), showing a relatively small kinetic barrier of 0.97 eV. This explains the poor O_2 tolerance of the Ru catalyst, which, along with its facile surface oxidation, results in it demonstrating the lowest activity (as shown in Fig. 4). The presence of O* at the adjacent sites weakened the adsorption energies for most cases, but the extent was dependent on the adsorbate and surface composition. The alloy surfaces exhibited adsorption energies between those of pure Ir and Ru surfaces. As expected, the adsorption energies of the Ir- and Ru-rich alloys tended to be closer to those of the pure Ir and Ru metals, respectively.

NO* can form intermediates through three processes: N* and O* by direct dissociation, N_2O* by recombination, and NO_2^* by oxidation. Similar to what was observed with the adsorption energies, the alloy surfaces exhibited intermediate reaction energies and activation barriers between those of the Ir and Ru surfaces in both the presence and absence of adjacent O*. Among the three possibilities of intermediate formation, NO* direct dissociation appeared to be the most favorable, showing exergonic behavior for all the clean surfaces. The endergonic energetics for the formation of N_2O and NO_2 in the absence of O_2 are consistent with the experimental results in which these intermediates were not detected (Fig. 1). The Ru and Ru-rich alloy surfaces showed favorable NO dissociation energies compared to the Ir and Ir-rich alloy surfaces. On the other hand, the Ir and Ir-rich alloy surfaces were calculated to be beneficial for the recombination (N_2O formation) and oxidation (NO_2 formation) of NO. This is due to the strong adsorption of NO and O on the Ru surface, resulting in bond-breaking reactions. If the Ru surface is crowded by adsorption species, bond-forming reactions, such as recombination and oxidation, may occur as on the Ir surface. In the presence of adjacent O*, NO* decomposition occurred more easily, while the formation of N_2O* and NO_2^* became more difficult, as shown in Table 2.

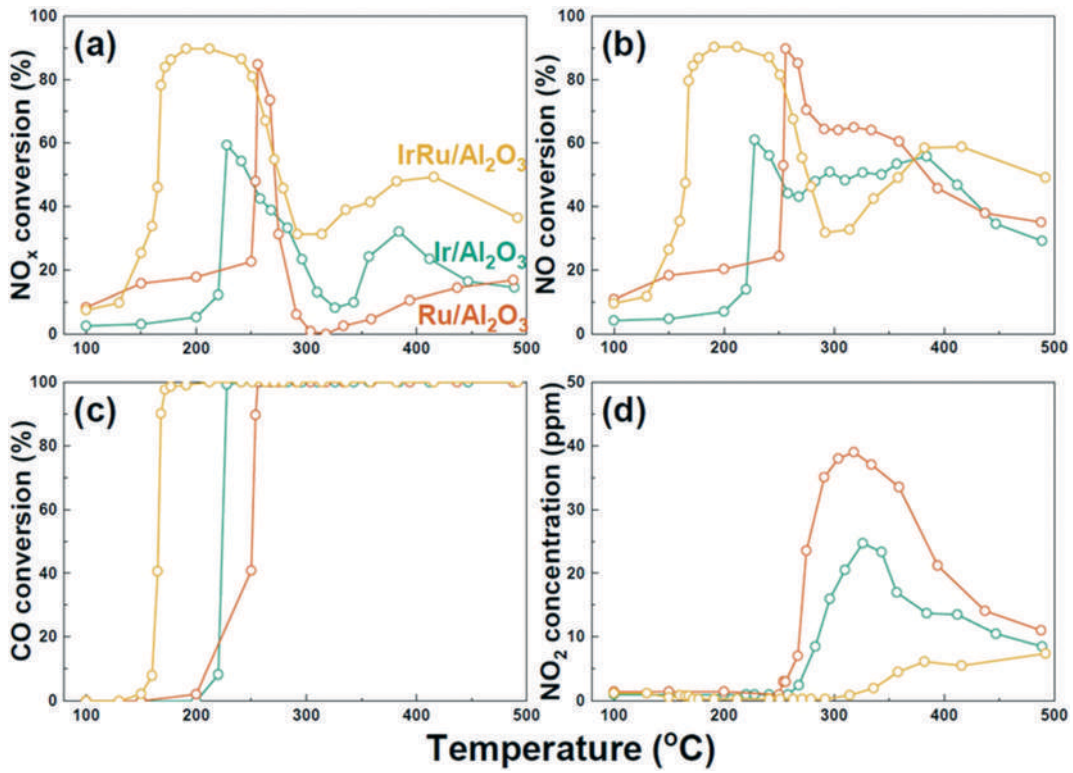

Fig. 4 NO reduction results obtained in the presence of O_2. (a) NO_x conversion, (b) NO conversion, (c) CO conversion, and (d) NO_2 concentration. Reaction conditions: T = 100–500 °C; P = 1 bar; 50 ppm NO, 0.7% CO, 5% O_2 balanced with N_2; GHSV = 100 000 h^{-1}.

Table 2 Reaction free energies and activation energies for possible reactions over Ir, Ir_3Ru_1, Ru_3Ir_1, and Ru surfaces (T = 200 °C; P = 1 bar)

		Reaction energy[a] (eV)							
		Clean				O*-Covered			
Reactions		Ir	Ir_3Ru_1	Ru_3Ir_1	Ru	Ir	Ir_3Ru_1	Ru_3Ir_1	Ru
Gas adsorption	NO(g) + * → NO*	−1.00	−1.23	−1.43	−1.70	−0.63	−1.08	−1.38	−1.66
	CO (g) + * → CO*	−0.73	−0.68	−0.56	−0.35	−0.50	−0.09	−0.31	−0.47
	O_2(g) + * → 2O*	−3.72 (1.31)	−3.44 (0.81)	−5.02 (0.97)	−5.96 (0.97)	−2.76 (1.06)	−3.71 (0.81)	−4.87 (1.01)	−5.81 (0.99)
NO dissociation	NO* → N* + O*	−1.05 (1.20)	−0.93 (0.76)	−1.85 (1.03)	−2.35 (0.90)	−0.44 (1.09)	−1.05 (0.99)	−1.78 (0.93)	−2.28 (0.87)
N_2O formation	NO* + N* → N_2O*	0.83 (1.56)	1.29 (1.83)	1.89 (1.97)	2.48 (2.62)	0.14 (1.10)	1.13 (1.83)	1.75 (2.07)	2.41 (2.47)
NO_2 formation	NO* + O* → NO_2^*	1.02 (0.70)	1.12 (1.51)	1.76 (2.47)	2.28 (2.45)	0.43 (0.36)	1.25 (1.51)	1.67 (1.94)	2.25 (2.67)
CO dissociation	CO* → C* + O*	1.59 (3.84)	1.53 (3.79)	1.06 (3.08)	−0.27 (2.38)	2.23 (4.24)	0.97 (3.79)	0.99 (3.28)	−0.03 (3.26)
NCO formation	N* + CO* → NCO*	1.19 (1.54)	1.05 (0.94)	0.88 (1.76)	0.67 (1.48)	0.72 (0.97)	0.36 (0.94)	0.58 (1.40)	0.80 (1.64)
CO oxidation	CO* + O* → CO_2(g)	−0.82 (1.49)	−1.01 (0.57)	−0.34 (1.09)	−0.08 (1.71)	−1.53 (0.60)	−1.47 (1.09)	−0.67 (1.16)	−0.03 (1.65)
N_2 formation	N_2O* → N_2(g) + O*	−3.13 (0.81)	−2.41 (0.94)	−3.83 (0.05)	−4.31 (0.28)	−2.83 (0.94)	−3.26 (0.69)	−3.26 (0.43)	−4.25 (0.12)
	N* + N* → N_2(g)	−1.25 (2.42)	−0.75 (2.22)	−0.08 (2.08)	0.52 (2.31)	−2.24 (2.39)	−1.08 (2.31)	−0.18 (2.24)	0.44 (2.20)
	N* + NO* → N_2(g) + O*	−2.30 (1.82)	−1.68 (1.95)	−1.94 (1.56)	−1.83 (1.28)	−2.69 (1.99)	−2.13 (1.75)	−2.13 (1.58)	−1.84 (1.44)

[a] Activation free energy for an individual reaction is provided in parentheses.

CO* can also form C* and O* by its direct decomposition and NCO* by its reaction with N*. CO_2 gas can be produced by simple CO* oxidation *via* reaction with O*, which is available as a result of the decomposition of NO*. Among these CO*-related reactions, CO_2 formation was the most favorable for all the catalysts, regardless of the presence of O* adatoms. Among the catalysts, the Ru surface exhibited the highest activation barrier with an endergonic reaction nature, while the Ir-containing catalysts offered spontaneous reaction thermodynamics with relatively low activation energy (E_a) barriers. This suggests that the Ru catalyst has poor activity for O* removal by the CO* oxidation reaction under both lean- and rich-burn conditions due to its high O* affinity. These reaction energetics explain the experimental CO oxidation results shown in Fig. 4(c), where CO oxidation had begun at low temperatures and the onset temperature of Ru/Al_2O_3 was retarded compared to those of the other catalysts. Since the direct CO dissociation reactions are thermodynamically unfavored on all the catalyst surfaces, they are not involved in the following mechanism study.

Finally, N_2 formation can occur through three reaction pathways: (1) N_2O dissociation, (2) N–N recombination, and (3) N–NO disproportionation. Although the N_2O dissociation exhibited very negative reaction energies with a small activation barrier, it may not be the main route of N_2 production because N_2O is very difficult to form, as discussed above. The reaction energies of the N–N recombination reactions are near zero and tend to become negative as the Ir content increases, but they show rather high activation energies ranging from 2.08 to 2.42 eV. The N_2 production through N–NO disproportionation reactions is highly exergonic on all the catalytic surfaces with lower activation barriers than those of the N–N recombination reactions. The O* produced *via* NO disproportionation can be removed by CO* oxidation with small kinetic barriers. The NO disproportionation reaction can be considered as the rate-determining step, as it showed the highest activation barrier among the reactions comprising the catalytic cycle of the CO-assisted NO reduction.

Reaction energy profiles were plotted (Fig. 5) by combining the most plausible routes for each of the reactants to observe how the reaction energetics changed throughout the catalytic cycle. In the case of the surface without O* adatoms (Fig. 5(a)), Ir shows weak NO and CO adsorption compared to Ru. Even though the overall reaction free energies are negative (spontaneous) for this reaction, the activation barriers for NO decomposition and N–N–O disproportionation appeared to primarily hinder the kinetics. This phenomenon is particularly noticeable for Ir, where the reactants are weakly adsorbed. The Ru surface offers strong binding for most of the adsorbates, which makes this catalyst inactive because of the difficult desorption energetics. The Ir_3Ru_1 and Ru_3Ir_1 alloy model surfaces exhibit intermediate energetics between those of the Ir and Ru surfaces for most of the elementary reactions. This suggests that alloy formation is beneficial in this reaction by providing modest adsorption strengths.

For the O*-covered surfaces (Fig. 5(b)), the overall energies along the reaction coordinate were shifted upward. In particular, the NO and CO adsorption reactions on the pure Ir and Ir-containing alloys were largely weakened compared to those on the pure Ru surface. This resulted in the alloy compounds exhibiting moderate energy levels to promote catalysis, which fell between those of the Ir and Ru surfaces.

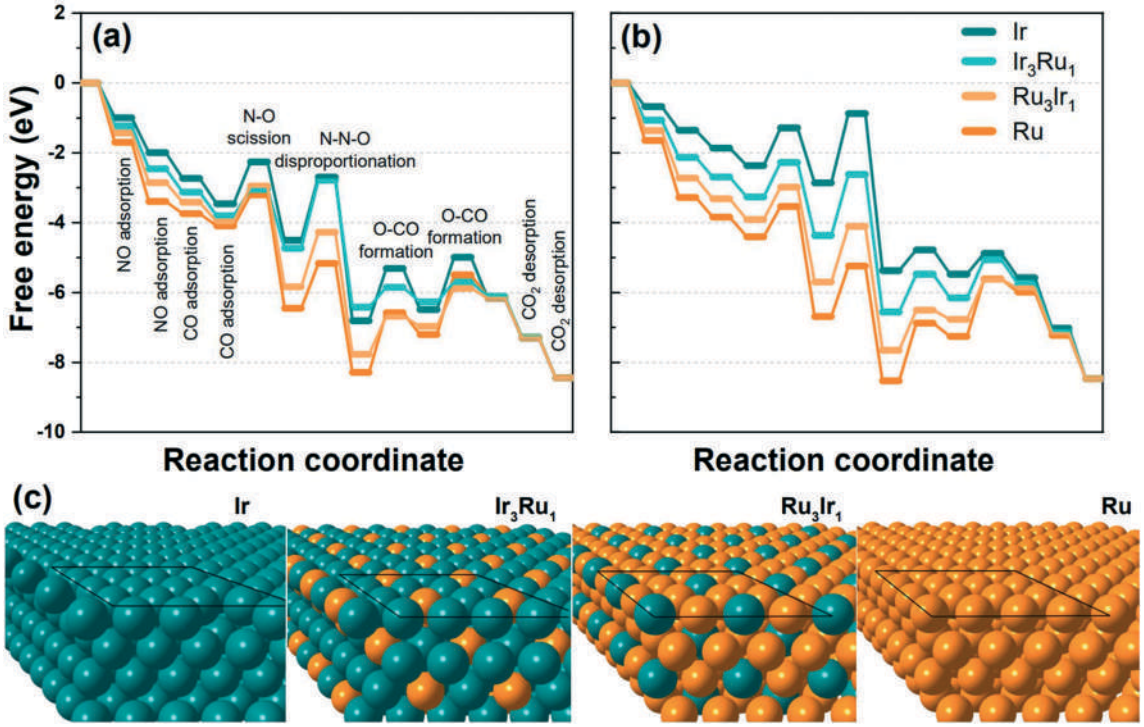

Fig. 5 Free energy profiles of NO reduction by CO (a) without and (b) with surface oxygen present. T = 200 °C and P = 0.1 MPa. (c) Structures of surface models. Solid squares indicate the unit cell.

The energy change caused by the presence of O* at neighboring sites on the surface nicely explains the experimental results shown in Fig. 3 and 4, where the alloy catalyst showed better NO_x removal performance than the pure Ir and Ru catalysts under lean-burn conditions. The energy changes of the four models under other conditions are shown in the ESI† (Fig. S9 and S10). To elucidate the origin of the alloy effect on the energy profile in the presence of neighboring O*, further DFT calculations were carried out using three different imaginary systems: ligand, strain, and ensemble.

3.4 Dominant effect of the alloyed surface

The alloying of metals may result in important changes in their catalytic activity and selectivity. Alloyed surfaces may demonstrate multiple effects at once; for instance, the hybridization of the electronic structure between two elements (ligand effect), changes in the tensile or compressive lattices (strain effect), and modifications of the adsorption configuration by altering the heterogeneity of the surface component (ensemble effect).[49] Because each of these effects can have a significant impact on the catalyst activity and selectivity, determining whether each effect is positive or negative would provide critical insight for designing more effective catalysts. In the present study, we constructed three different structures to characterize the three aforementioned effects and determined which one predominantly influenced the IrRu alloy structure (see Fig. S8 in the ESI†).

To simulate the alloy surface where only the ligand effect is observed, the second layer of the Ir slab was replaced with Ru and *vice versa*. In the case of the strain-applied model, the lattices of pure Ir and Ru slabs were compressed by 2.06% and elongated by 0.58%, respectively, according to the DFT-optimized bulk alloy structures. The ensemble effect can be studied by modelling several surface geometries,[56] but in this study, we simply doped the counter-metal monomer into the surface layer of the host slab. The ligand, strain, and ensemble effects on the NO reduction energetics in the presence of O* adatoms are illustrated in Fig. 6, where the directions of the changes in binding energy are indicated by arrows based on the adsorption strength of NO and CO.

Fig. 6(a) shows the reaction energy changes induced by the ligand effect. On the Ir surface, where the second layer was substituted with Ru (Ir–Ru_{lig}), the overall energies shifted upward with respect to pure Ir, indicating weakened binding energies. In contrast, the Ru–Ir_{lig} model showed bolstered adsorption. These phenomena can be explained by the charge transfer from Ru to Ir, which was confirmed by Bader charge analysis[57] (Fig. S1 and S2†). For instance, the increase in the Ir charge density led to a downshift of its d-band center and lowered the number of electrons donated and back-donated between the Ir metal and adsorbed CO (or NO).[58,59]

The strain-applied models (Fig. 6(b)) showed similar trends to the ligand models. The Ir model with compressive strain (Ir_{strain}) showed binding energies for NO and CO that were weaker than those provided by the parent-Ir models.

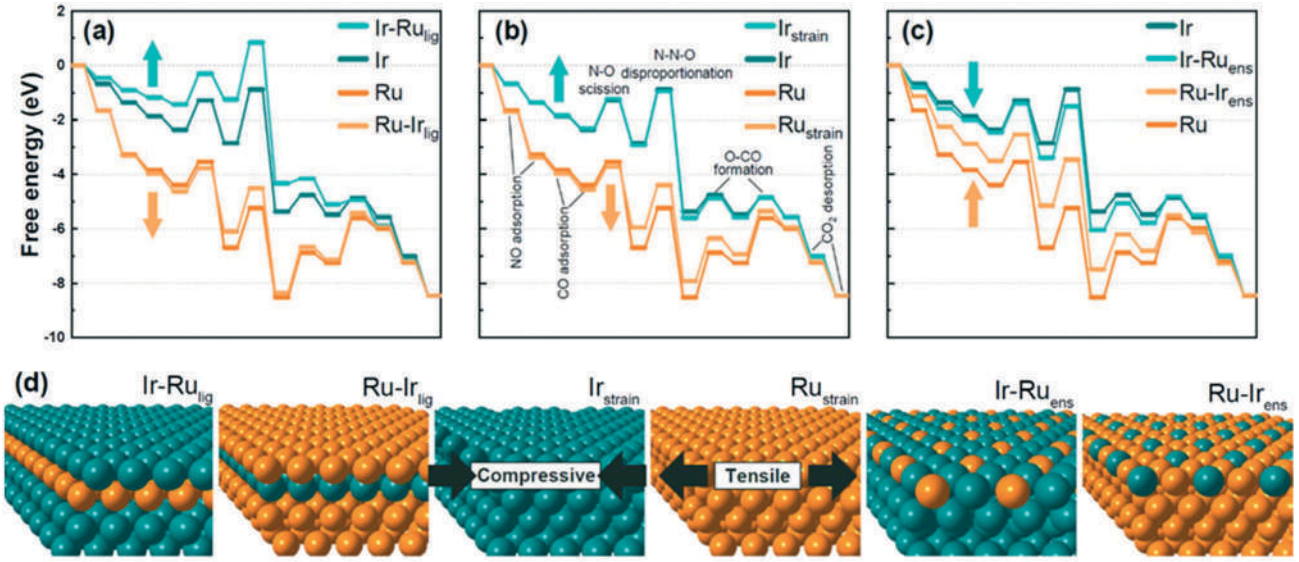

Fig. 6 Subdivided effects of alloy formation on the CO-assisted NO reduction in the presence of O* adatoms. (a) Ligand effect, (b) strain effect, and (c) ensemble effect. Surface models are shown in (d). T = 200 °C and P = 0.1 MPa. The green and orange arrows indicate the adsorption energy shift on Ir and Ru, respectively, induced by the alloying effects.

Contrastingly, the Ru model with tensile strain (Ru_{strain}) showed stronger binding energies than the parent-Ru models. These findings are consistent with previous reports,[37,38,60,61] which also stated that compressive and tensile strains applied to transition metals weakened and strengthened their binding energies to adsorbates, respectively. This is likely because of the alterations in the surface electronic structure.

In the case of the surface ensemble model (Fig. 6(c)), the energy changes were mostly the opposite of those shown by the previous two cases. That is, the Ir surface doped with a Ru monomer ($Ir–Ru_{ens}$) showed stronger binding energies for NO and CO than the pure Ir surface, while the Ru surface doped with an Ir monomer ($Ru–Ir_{ens}$) showed weaker binding energies for the same adsorbates than the pure Ru surface. As a result, the reaction energy profiles of both ensemble

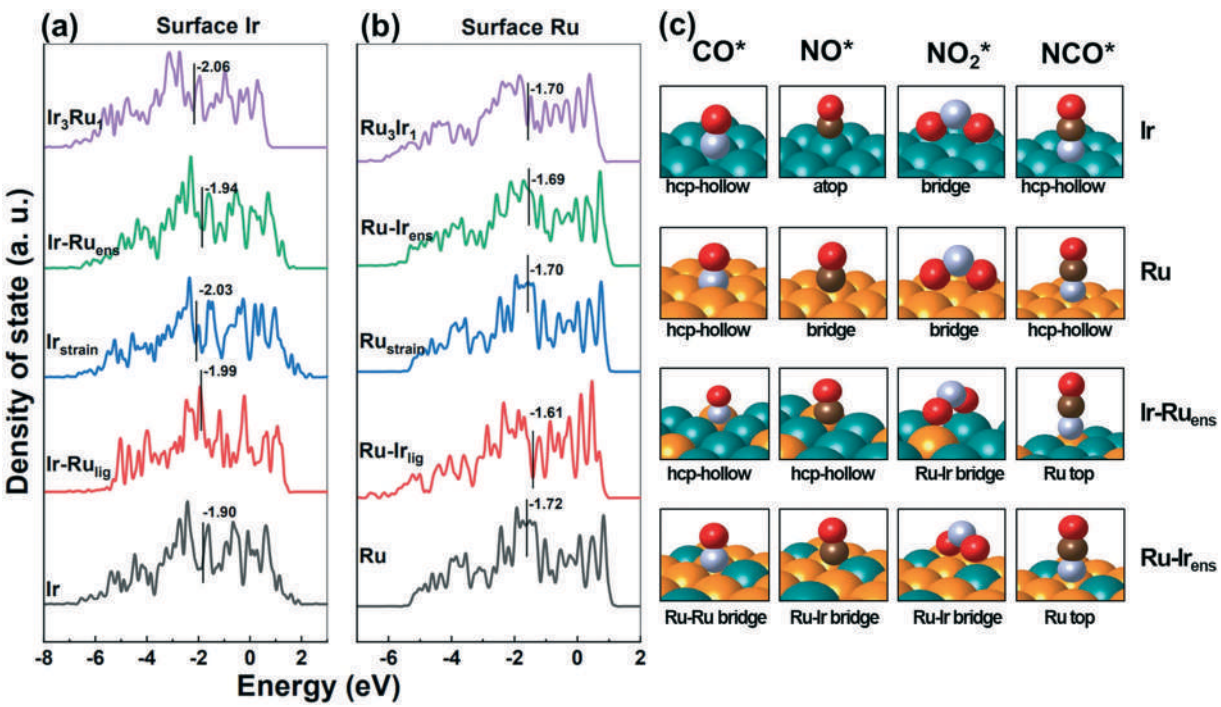

Fig. 7 Local density of states projected onto the d-band of (a) surface Ir and (b) surface Ru atoms. Band centers are indicated. (c) Configurations of reactants and intermediates on pure metal surfaces and ensemble-model surfaces.

models were located between pure Ir and Ru, which are almost identical to those of the bulk alloy models (Fig. 5(b)).

The energy changes of the three models under other conditions are shown in the ESI† (Fig. S11–S19). It is noteworthy that the trends of energy change are all similar regardless of the reaction temperature or the presence of surface oxygen.

The d-band centers of the surface Ir and Ru atoms are shown in Fig. 7(a) and (b), respectively. As expected from the direction of the binding energy shift (Fig. 6 and discussion above), the d-band center of the surface Ir moved down as the ligand and strain effects were applied, which resulted in the weakened adsorption. In contrast, the alloying effects showed an upshift of the Ru d-band, strengthening the adsorption. We note that the d-band shifts due to the ensemble effect were not that significant compared to the other two. Instead, as shown in Fig. 7(c), the surface heterogeneity changed the adsorption mode of the adsorbates, which affects the adsorption energy in a different way than the d-band shift does.

In Fig. 6(a) and (b), the energy of some reactions changed in a different direction than the NO and CO binding energies. Quantifying the extent of energy change along with the overall reaction path may help to identify how much each effect contributes to the catalytic performance. We assumed that the ideal IrRu alloy would show an energy profile located exactly on the median values (E_{mid}) of pure Ir and Ru catalysts. The mean energy differences between the E_{mid} and the energy value of each alloy model with and without neighboring O* are shown in Fig. 8(a) and (b), respectively.

Among the various alloy models, Ru–Ir_{ens} showed the closest energetics to the E_{mid} with a mean difference of −0.07 and −0.22 eV in the absence and presence of neighboring O*, respectively. Models in which the ligand or strain effects were applied did not necessarily reduce the difference between their energy levels and the E_{mid} value. For instance, the Ir_3-Ru_1 and Ru_3Ir_1 models, where ligand, strain, and ensemble effects were implemented together, showed energy levels that were largely different from the E_{mid} value. Furthermore, this difference was larger than that between the E_{mid} value and the energy level of the Ru–Ir_{ens} model that only employed the ensemble effect. Accordingly, the superior performance of the experimentally synthesized IrRu alloy catalyst for CO-SCR is mostly due to the ensemble effect.

We note that the ensemble model also includes ligand effects. However, when only the ligand effect occurred

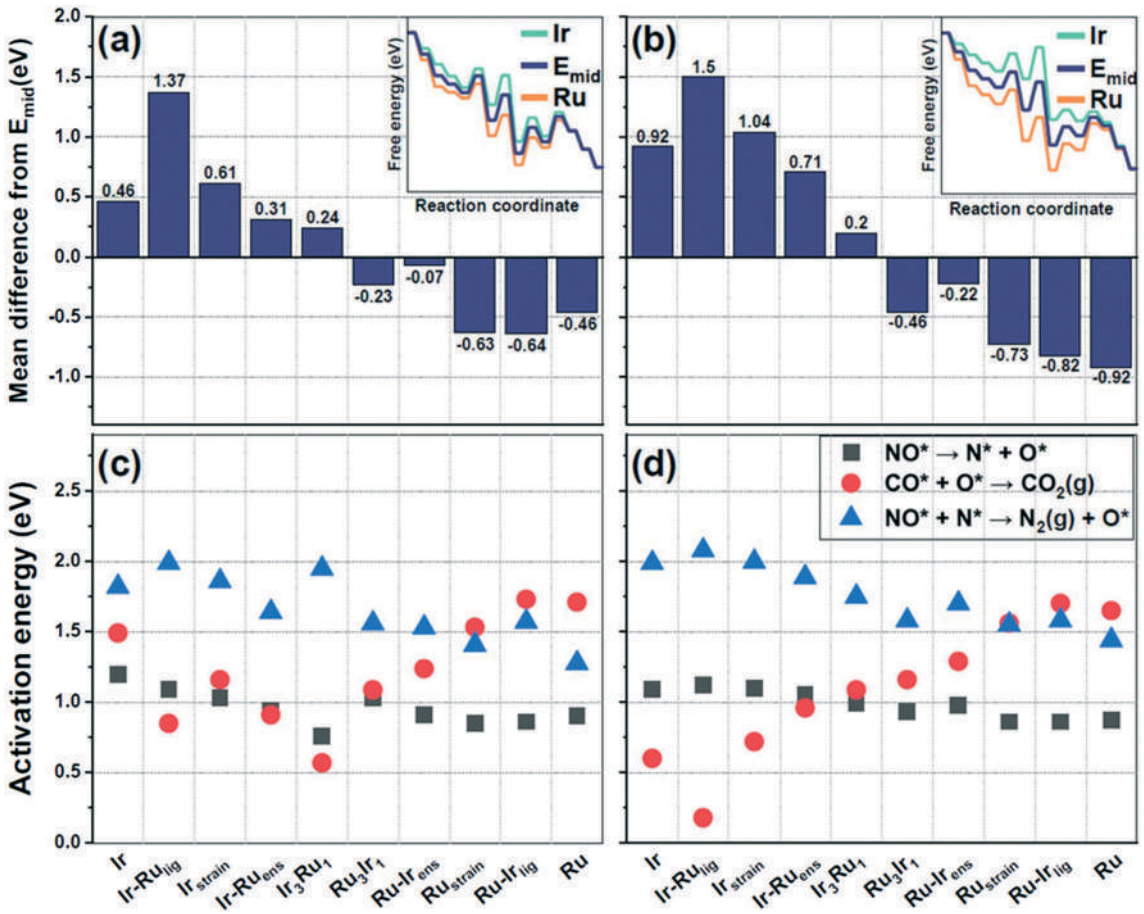

Fig. 8 Mean difference between the median values (E_{mid}) of the pure Ir and Ru catalysts and the energy values of the different alloy surfaces (a) without and (b) with surface oxygen present. Activation energy (E_a) trends for the three important reactions among the different catalytic models (c) without and (d) with surface oxygen present. T = 200 °C and P = 0.1 MPa.

independently, the overall energy profile (Fig. 6(a)) and the resulting kinetic barrier (Fig. 8) did not change toward accelerating the catalytic reaction. Therefore, the effect of promoting the catalytic reaction by the alloy formation is mostly due to the surface ensemble.

The activation energy (E_a) values among the catalytic models for the three important elementary reactions of CO-SCR, including N–O dissociation, CO–O oxidation, and N–NO disproportionation, are illustrated in the absence and presence of surface oxygen in Fig. 8(c) and (d), respectively. Regardless of the presence of surface oxygen, N–NO disproportionation appeared to determine the overall reaction rates for most of the catalyst surfaces. However, the Ru, Ru–Ir_{lig}, and Ru_{strain} models showed the highest barriers to CO–O oxidation. Since the E_a exponentially affects the reaction rate, it is better to have evenly moderate kinetic barriers for several stages than to have a particularly high kinetic barrier for one specific reaction. For example, the reaction rate of Ru_3Ir_1, which has comparable E_a among reactions, will be faster than that of Ir, whose N–NO reaction clearly limits its reaction rate. In this context, it can be expected that alloy catalysts with an ensemble effect will be advantageous for the CO-SCR reaction. The energy changes of the models under other conditions are shown in the ESI† (Fig. S20–S23).

Summarizing the above results, the improved CO-SCR performance of the IrRu alloy catalyst is due to the effect of counter metals present on the surface rather than the effects of ligands or strain. That is, changes in the electron density due to ligands or strain are detrimental to the catalyst performance. However, the presence of a surface heteroatom alters the adsorption configurations and improves the catalytic performance.

4. Conclusion

We synthesized Ir/Al_2O_3, Ru/Al_2O_3, and $IrRu/Al_2O_3$ catalysts using a wetness impregnation method and studied the reaction performance of NO reduction by CO in the presence and absence of O_2. $IrRu/Al_2O_3$ shows excellent catalytic activity under lean (O_2-rich) burn conditions and offers high NO_x conversion as well as good N_2 and CO_2 selectivity. To investigate its intrinsic activity (*ca.* 90% NO_x conversion at 200 °C), we examined the catalyst structure using HR-PXRD and HR-TEM characterization techniques and confirmed the $IrRu/Al_2O_3$ alloy catalyst formation. To understand the mechanism behind the catalyst activity, we performed DFT calculations for all the viable elementary steps and drew their energetics. From the DFT energetics, we came to understand that the IrRu alloy offered optimal energetics for NO reduction by CO under O_2-rich conditions, promoted NO dissociation, and suppressed side reactions, such as NO_2 and N_2O formation. This resulted in high N_2 selectivity *via* the NO disproportionation reaction pathway. The DFT calculations also showed that the IrRu catalyst promoted the CO oxidation reaction with a low E_a barrier, which is the key elementary step for low-temperature CO-SCR. By stimulating the CO oxidation reaction, the IrRu catalyst also improved its O_2 tolerance even though O_2 dissociation was still favorable. The poor O_2 tolerance was the main reason for the low activity of the Ru/Al_2O_3 catalyst, where the active site was occupied by surface O* species. Moreover, the DFT calculations revealed that the ensemble effect plays a key role in promoting the reactivity of the IrRu alloy. Based on this study, we suggest that making the IrRu surface alloy is better for CO-SCR than forming an alloy over the bulk structure. Employing this idea could provide catalysts that efficiently reduce NO with minimal use of precious metals.

Author contributions

The manuscript was written through contributions of all authors. All authors have given approval to the final version of the manuscript.

Conflicts of interest

There are no conflicts to declare.

Acknowledgements

This work was supported by the Institutional Research Program of KRICT (SI2061-22) and KIST (2E31340-21-P011). Also, this work was performed as part of the Technology Development Program to Solve Climate Changes through the National Research Foundation of Korea (NRF) funded by the Ministry of Science, ICT (NRF-2019M1A2A2103855).

References

1 S. Roy and A. Baiker, NOx Storage–Reduction Catalysis: From Mechanism and Materials Properties to Storage –Reduction Performance, *Chem. Rev.*, 2009, **109**(9), 4054–4091.
2 Y. Cheng, J. Liu, Z. Zhao, Y. Wei, W. Song and C. Xu, The simultaneous purification of PM and NOx in diesel engine exhausts over a single 3DOM $Ce_{0.9-x}Fe_{0.1}Zr_xO_2$ catalyst, *Environ. Sci.: Nano*, 2017, **4**(5), 1168–1177.
3 X. Chen, P. Wang, P. Fang, H. Wang, C. Cen, W. Zeng and Z. Wu, Design strategies for SCR catalysts with improved N_2 selectivity: the significance of nano-confining effects by titanate nanotubes, *Environ. Sci.: Nano*, 2017, **4**(2), 437–447.
4 X. Chen, Y. Xiong, W. Zou, L. Zhang, S. Wu, X. Dong, F. Gao, Y. Deng, C. Tang, Z. Chen, L. Dong and Y. Chen, Correlation between the physicochemical properties and catalytic performances of $Ce_xSn_{1-x}O_2$ mixed oxides for NO reduction by CO, *Appl. Catal., B*, 2014, **144**(1), 152–165.
5 Y. J. Kim, J. K. Lee, K. M. Min, S. B. Hong, I. S. Nam and B. K. Cho, Hydrothermal stability of CuSSZ13 for reducing NOx by NH_3, *J. Catal.*, 2014, **311**, 447–457.
6 I. A. Resitoglu and A. Keskin, Hydrogen applications in selective catalytic reduction of NOx emissions from diesel engines, *Int. J. Hydrogen Energy*, 2017, **42**(36), 23389–23394.

7 X. Y. Wang, W. Wen, J. X. Mi, X. X. Li and R. H. Wang, The ordered mesoporous transition metal oxides for selective catalytic reduction of NOx at low temperature, *Appl. Catal., A*, 2015, **176**, 454–463.
8 H. Hamada and M. Haneda, A review of selective catalytic reduction of nitrogen oxides with hydrogen and carbon monoxide, *Appl. Catal., A*, 2012, **421–422**, 1–13.
9 I. Heo, S. Sung, M. B. Park, T. S. Chang, Y. J. Kim, B. K. Cho, S. B. Hong, J. W. Choung and I.-S. Nam, Effect of Hydrocarbon on DeNOx Performance of Selective Catalytic Reduction by a Combined Reductant over Cu-Containing Zeolite Catalysts, *ACS Catal.*, 2019, **9**(11), 9800–9812.
10 E. Shim, H. Park and C. Bae, Comparisons of advanced combustion technologies (HCCI, PCCI, and dual-fuel PCCI) on engine performance and emission characteristics in a heavy-duty diesel engine, *Fuel*, 2020, **262**, 116436.
11 M. Iwamoto and H. Hamada, Removal of nitrogen monoxide from exhaust gases through novel catalytic processes, *Catal. Today*, 1991, **10**(1), 57–71.
12 G. Zhang, T. Yamaguchi, H. Kawakami and T. Suzuki, Selective reduction of nitric oxide over platinum catalysts in the presence of sulfur dioxide and excess oxygen, *Appl. Catal., B*, 1992, **1**(3), L15–L20.
13 R. Burch, P. J. Millington and A. P. Walker, Mechanism of the selective reduction of nitrogen monoxide on platinum-based catalysts in the presence of excess oxygen, *Appl. Catal., B*, 1994, **4**(1), 65–94.
14 S. I. Matsumoto, Catalytic Reduction of Nitrogen Oxides in Automotive Exhaust Containing Excess Oxygen by NOx Storage-Reduction Catalyst, *CATTECH*, 2000, **4**(2), 102–109.
15 Q. Zhang, L. Lv, J. Zhu, X. Wang, J. Wang and M. Shen, The effect of CO on NO reduction over Pt/Pd-based NSR catalysts at low temperature, *Catal. Sci. Technol.*, 2013, **3**(4), 1069–1077.
16 D. Na-Ranong, R. Yuangsawad, P. Kitchaiya and T. Aida, Application of periodic operation to kinetic study of NO–CO reaction over Rh/Al_2O_3, *Chem. Eng. J.*, 2009, **146**(2), 275–286.
17 A. Srinivasan and C. Depcik, Review of Chemical Reactions in the NO Reduction by CO on Rhodium/Alumina Catalysts, *Catal. Rev.: Sci. Eng.*, 2010, **52**(4), 462–493.
18 J. Jeon, K.-I. Kon, T. Toyao, K.-I. Shimizu and S. Furukawa, Design of Pd-based pseudo-binary alloy catalysts for highly active and selective NO reduction, *Chem. Sci.*, 2019, **10**(15), 4148–4162.
19 J. Shibata, M. Hashimoto, K.-I. Shimizu, H. Yoshida, T. Hattori and A. Satsuma, Factors Controlling Activity and Selectivity for SCR of NO by Hydrogen over Supported Platinum Catalysts, *J. Phys. Chem. B*, 2004, **108**(47), 18327–18335.
20 W. An, Q. Zhang, K. T. Chuang and A. R. A. Sanger, Hydrophobic Pt/Fluorinated Carbon Catalyst for Reaction of NO with NH_3, *Ind. Eng. Chem. Res.*, 2002, **41**(1), 27–31.
21 R. Burch, J. P. Breen and F. C. Meunier, A review of the selective reduction of NOx with hydrocarbons under lean-burn conditions with non-zeolitic oxide and platinum group metal catalysts, *Appl. Catal., B*, 2002, **39**(4), 283–303.
22 S. J. Tauster and L. L. Murrell, The NO–CO reaction in the presence of excess O_2 as catalyzed by iridium, *J. Catal.*, 1976, **41**(1), 192–195.
23 M. Ogura, A. Kawamura, M. Matsukata and E. Kikuchi, Catalytic Activity of Ir for NO-CO Reaction in the Presence of SO_2 and Excess Oxygen, *Chem. Lett.*, 2000, **29**(2), 146–147.
24 M. Shimokawabe, M. Niitsu, H. Inomata, N. Iwasa and M. A. Arai, Highly Active Ir/WO_3 Catalyst for the Selective Reduction of NO by CO in the Presence of O_2 or O_2 + SO_2, *Chem. Lett.*, 2005, **34**(10), 1426–1427.
25 H. Inomata, M. Shimokawabe and M. Arai, An Ir/WO_3 catalyst for selective reduction of NO with CO in the presence of O_2 and/or SO_2, *Appl. Catal., A*, 2007, **332**(1), 146–152.
26 M. Haneda, T. Yoshinari, K. Sato, Y. Kintaichi and H. Hamada, Ir/SiO_2 as a highly active catalyst for the selective reduction of NO with CO in the presence of O_2 and SO_2, *Chem. Commun.*, 2003(22), 2814–2815.
27 J. H. Song, D. C. Park, Y.-W. You, T. S. Chang, I. Heo and D. H. Kim, Lean NOx reduction by CO at low temperature over bimetallic $IrRu/Al_2O_3$ catalysts with different Ir : Ru ratios, *Catal. Sci. Technol.*, 2020, **10**(7), 2120–2136.
28 I. Heo, Y.-W. You, J. H. Lee, S. J. Schmieg, D. Y. Yoon and C. H. Kim, Urealess NOx Reduction by Carbon Monoxide in Simulated Lean-Burn Exhausts, *Environ. Sci. Technol.*, 2020, **54**(13), 8344–8351.
29 Y.-W. You, Y. J. Kim, J. H. Lee, M. W. Arshad, S. K. Kim, S. M. Kim, H. Lee, L. T. Thompson and I. Heo, Unraveling the origin of extraordinary lean NOx reduction by CO over Ir-Ru bimetallic catalyst at low temperature, *Appl. Catal., B*, 2021, **280**, 119374.
30 J. H. Holles, R. J. Davis, T. M. Murray and J. M. Howe, Effects of Pd Particle Size and Ceria Loading on NO Reduction with CO, *J. Catal.*, 2000, **195**(1), 193–206.
31 J. H. Holles, M. A. Switzer and R. J. Davis, Influence of Ceria and Lanthana Promoters on the Kinetics of NO and N2O Reduction by CO over Alumina-Supported Palladium and Rhodium, *J. Catal.*, 2000, **190**(2), 247–260.
32 M. Kantcheva, O. Samarskaya, L. Ilieva, G. Pantaleo, A. M. Venezia and D. Andreeva, In situ FT-IR investigation of the reduction of NO with CO over Au/CeO_2-Al_2O_3 catalyst in the presence and absence of H2, *Appl. Catal., B*, 2009, **88**(1), 113–126.
33 Z.-P. Liu, S. J. Jenkins and D. A. King, Step-Enhanced Selectivity of NO Reduction on Platinum-Group Metals, *J. Am. Chem. Soc.*, 2003, **125**(48), 14660–14661.
34 Z.-P. Liu, S. J. Jenkins and D. A. King, Car Exhaust Catalysis from First Principles: Selective NO Reduction under Excess O_2 Conditions on Ir, *J. Am. Chem. Soc.*, 2004, **126**(34), 10746–10756.
35 V. S. Marakatti and S. C. Peter, Synthetically tuned electronic and geometrical properties of intermetallic compounds as effective heterogeneous catalysts, *Prog. Solid State Chem.*, 2018, **52**, 1–30.
36 F. Steffler, G. F. De Lima and H. A. Duarte, The effect of the heteroatom (X=P, As, Si and Ge) on the geometrical and

electronic properties of α-Keggin polyoxometalates (M=Mo, W and Nb) – A DFT investigation, *J. Mol. Struct.*, 2020, **1213**, 128159.

37 K. Yan, S. K. Kim, A. Khorshidi, P. R. Guduru and A. A. Peterson, High Elastic Strain Directly Tunes the Hydrogen Evolution Reaction on Tungsten Carbide, *J. Phys. Chem. C*, 2017, **121**(11), 6177–6183.

38 S. J. Kim and S. K. A. Jang, Slow Strain Rate Test Experiment to Evaluate the Characteristics of High-Strength Al-Mg Alloy for Application in Ships, *Mater. Sci. Forum*, 2006, **510–511**, 162–165.

39 T. Adit Maark and A. A. Peterson, Understanding Strain and Ligand Effects in Hydrogen Evolution over Pd(111) Surfaces, *J. Phys. Chem. C*, 2014, **118**(8), 4275–4281.

40 G. Kresse and J. Furthmüller, Efficiency of ab-initio total energy calculations for metals and semiconductors using a plane-wave basis set, *Comput. Mater. Sci.*, 1996, **6**, 15–50.

41 G. Kresse and J. Hafner, Ab initio molecular-dynamics simulation of the liquid-metal–amorphous-semiconductor transition in germanium, *Phys. Rev. B: Condens. Matter Mater. Phys.*, 1994, **49**(20), 14251–14269.

42 M. Dion, H. Rydberg, E. Schröder, D. C. Langreth and B. I. Lundqvist, Van der Waals Density Functional for General Geometries, *Phys. Rev. Lett.*, 2004, **92**(24), 246401.

43 J. Klime, D. R. Bowler and A. Michaelides, Van der Waals density functionals applied to solids, *Phys. Rev. B: Condens. Matter Mater. Phys.*, 2011, **83**, 1–13.

44 K. Lee, É. D. Murray, L. Kong, B. I. Lundqvist and D. C. Langreth, Higher-accuracy van der Waals density functional, *Phys. Rev. B: Condens. Matter Mater. Phys.*, 2010, **82**(8), 081101.

45 C. J. Cramer, *Essentials of computational chemistry: Theories and models*, John Wiley & Sons, 2nd edn, 2004.

46 C. Liu, L. Zhu, X. Wen, Y. Yang, Y.-W. Li and H. Jiao, Hydrogen Adsorption on Ir(111), Ir(100) and Ir(110) Surface and Coverage Dependence, *Surf. Sci.*, 2020, **692**, 121514.

47 R. B. Barros, A. R. Garcia and L. M. Ilharco, Effect of Oxygen Precoverage on the Reactivity of Methanol on Ru(001) Surfaces, *J. Phys. Chem. B*, 2004, **108**(15), 4831–4839.

48 N. Takehiro, P. Liu, A. Bergbreiter, J. K. Nørskov and R. J. Behm, Hydrogen adsorption on bimetallic PdAu(111) surface alloys: minimum adsorption ensemble, ligand and ensemble effects, and ensemble confinement, *Phys. Chem. Chem. Phys.*, 2014, **16**(43), 23930–23943.

49 H. Li, K. Shin and G. Henkelman, Effects of ensembles, ligand, and strain on adsorbate binding to alloy surfaces, *J. Chem. Phys.*, 2018, **149**(17), 174705.

50 G. Henkelman, B. P. Uberuaga and H. Jónsson, A climbing image nudged elastic band method for finding saddle points and minimum energy paths, *J. Chem. Phys.*, 2000, **113**(22), 9901–9904.

51 P. Xiao, D. Sheppard, J. Rogal and G. Henkelman, Solid-state dimer method for calculating solid-solid phase transitions, *J. Chem. Phys.*, 2014, **140**(17), 174104.

52 J. Kästner and P. Sherwood, Superlinearly converging dimer method for transition state search, *J. Chem. Phys.*, 2008, **128**(1), 014106.

53 H. E. Swanson, N. T. Gilfrich and G. M. Ugrinic, Standard X-ray diffraction powder patterns, *Natl. Bur. Stand. Circ.*, 1955, **539**(5), 1–75.

54 E. O. Hall and J. Crangle, An X-ray investigation of the reported high-temperature allotropy of ruthenium, *Acta Crystallogr.*, 1957, **10**, 240–241.

55 X. Zhang, X. Cheng, C. Ma and Z. Wang, Effects of the Fe/Ce ratio on the activity of CuO/CeO_2–Fe_2O_3 catalysts for NO reduction by CO, *Catal. Sci. Technol.*, 2018, **8**(13), 3336–3345.

56 Y. Wang, L. Cao, N. J. Libretto, X. Li, C. Li, Y. Wan, C. He, J. Lee, J. Gregg, H. Zong, D. Su, J. T. Miller, T. Mueller and C. Wang, Ensemble Effect in Bimetallic Electrocatalysts for CO_2 Reduction, *J. Am. Chem. Soc.*, 2019, **141**(42), 16635–16642.

57 R. F. W. Bader, *Atoms in Molecules: A Quantum Theory*, Oxford University Press, Oxford, UK, 1990.

58 B. Hammer, Y. Morikawa and J. K. Nørskov, CO Chemisorption at Metal Surfaces and Overlayers, *Phys. Rev. Lett.*, 1996, **76**(12), 2141–2144.

59 Z.-H. Zeng, J. L. F. Da Silva and W.-X. Li, Theory of nitride oxide adsorption on transition metal (111) surfaces: a first-principles investigation, *Phys. Chem. Chem. Phys.*, 2010, **12**(10), 2459–2470.

60 X. Cheng, L. Jiang, Y. Li, H. Zhang, C. Hu, S. Xie, M. Liu and Z. Qi, Using strain to alter the energy bands of the monolayer $MoSe_2$: A systematic study covering both tensile and compressive states, *Appl. Surf. Sci.*, 2020, **521**, 146398.

61 H. Alavi-Rad, A. Kiani-Sarkaleh, S. Rouhi and A. Ghadimi, Investigation of the electronic and thermoelectric properties of hydrogenated monolayer germanene under biaxial tensile and compressive strains by DFT approach, *Phys. E*, 2020, **124**, 114339.

